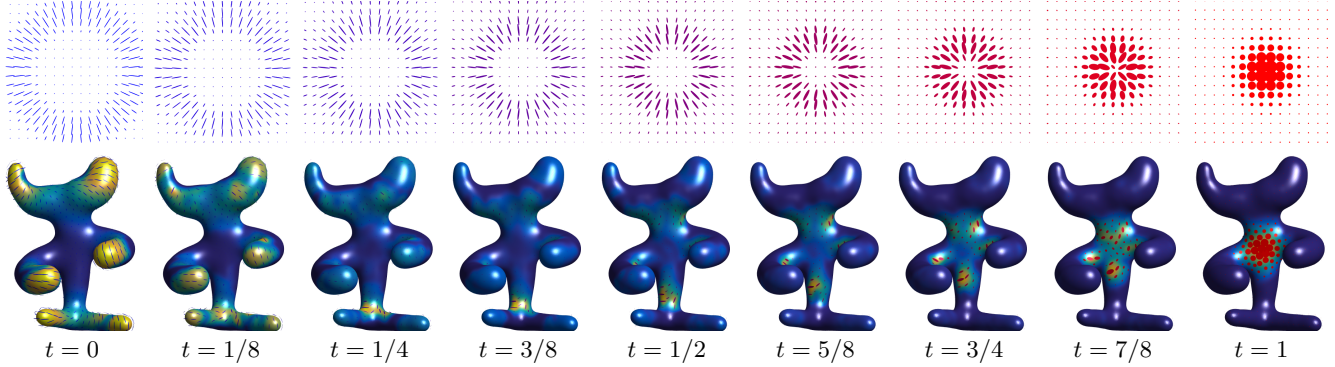


# Quantum Optimal Transport for Tensor Field Processing



**Figure 1:** Given two input fields of positive semidefinite matrices (displayed at times  $t \in \{0, 1\}$  using ellipses) on some domain (here, a 2-D planar square and a surface mesh), our Quantum Optimal Transport (Q-OT) method defines a continuous interpolating path for  $t \in [0, 1]$ . Unlike linear interpolation schemes, Q-OT transports the “mass” of the tensors (size of the ellipses) as well as their anisotropy and orientation. This interpolation, and its extension to finding the barycenter of several input fields, is computed using a fast extension of the well-known Sinkhorn algorithm.

## 1 Abstract

This article introduces a new notion of optimal transport (OT) between tensor fields, which are measures whose values are positive semidefinite (PSD) matrices. This “quantum” formulation of OT (Q-OT) corresponds to a relaxed version of the classical Kantorovich transport problem, where the fidelity between the input PSD-valued measures is captured using the geometry of the Von-Neumann quantum entropy. We propose a quantum-entropic regularization of the resulting convex optimization problem, which can be solved efficiently using an iterative scaling algorithm. This method is a generalization of the celebrated Sinkhorn algorithm to the quantum setting of PSD matrices. We extend this formulation and the quantum Sinkhorn algorithm to compute barycenters within a collection of input tensor fields. We illustrate the usefulness of the proposed approach on applications to procedural noise generation, anisotropic meshing, diffusion tensor imaging and spectral texture synthesis.

**Keywords:** Optimal transport, tensor field, PSD matrices, quantum entropy

**Concepts:** •Computing methodologies → Shape analysis;

## 1 Introduction

Optimal transport (OT) is an active field of research at the intersection of probability theory, PDEs, convex optimization and numerical analysis. OT offers a canonical way to lift a ground distance on some metric space to a metric between arbitrary probability measures defined over this base space. OT distances offer many interesting features, and in particular lead to a geometrically faithful way to manipulate and interpolate probability distributions.

Permission to make digital or hard copies of part or all of this work for personal or classroom use is granted without fee provided that copies are not made or distributed for profit or commercial advantage and that copies bear this notice and the full citation on the first page. Copyrights for third-party components of this work must be honored. For all other uses, contact the owner/author(s). © 2017 Copyright held by the owner/author(s).

### 28 1.1 Previous Work

**29 Scalar-valued optimal transport.** Dating back to the eighteenth century, classical instances of the optimal transport problem seek 30 a minimal-cost matching between two distributions defined over 31 a geometric domain, e.g. matching supply to demand while incurring 32 minimal cost. Initially formulated by Monge in terms of an 33 unknown map transporting mass [1781], its reformulation by Kan- 34 torovich [1942] as a linear program (static formulation) enables the 35 use of convex analysis to study its structure and develop numerical 36 solvers. The equivalence between these two formulations was 37 introduced by Brenier [1991] and opened the door to a dynamical 38 (geodesic) reformulation [Benamou and Brenier 2000]. We refer 39 to [Santambrogio 2015] for a review of the theoretical foundations 40 of OT.

The basic OT problem has been extended in various ways, a typical 42 illustration of which being the computation of a barycenter (Fréchet 43 mean) of input measures, a convex program studied by Aguech and 44 Carlier [2011]. OT has found numerous applications, for instance in 45 computer vision (under the name “earth mover distance”) [Rubner 46 et al. 2000] or computer graphics [Bonneel et al. 2011].

**48 Unbalanced transport.** While the initial formulations of OT are 49 restricted to positive measures of equal mass (normalized probability 50 distributions), a recent wave of activity has proposed and studied 51 a family of “canonical” extensions to the “unbalanced” setting of 52 arbitrary positive measures. This covers both a dynamic formulation 53 [Liero et al. 2016; Kondratyev et al. 2015; Chizat et al. 2016b] 54 and a static one [Liero et al. 2015; Chizat et al. 2015] and has been 55 applied in machine learning [Frogner et al. 2015]. Our work extends 56 this static unbalanced formulation to tensor-valued measures.

**57 Entropic regularization.** The current state-of-the-art OT approx- 58 imation for arbitrary ground costs uses entropic regularization of 59 the transport plan. This leads to strictly convex programs that can 60 be solved using a simple class of highly parallelizable “diagonal 61 scaling” algorithms. The landmark paper of Cuturi [2013] inspired 62 detailed study of these solvers, leading to various generalizations 63 of Sinkhorn’s algorithm [1964]. This includes for instance the use

fast convolutional structures [Solomon et al. 2015], extensions to barycenters [Benamou et al. 2015] and to unbalanced OT [Frogner et al. 2015; Chizat et al. 2016a]. These entropic regularization techniques correspond to the use of projection and proximal maps for the Kullback–Leibler Bregman divergence and are equivalent to iterative projections [Bregman 1967] and Dykstra’s algorithm [Dykstra 1983; Bauschke and Lewis 2000]. An important contribution of the present work is to extend these techniques to the matrix setting (i.e., using quantum divergences). Note that quantum divergences have been recently used to solve some machine learning problems [Dhillon and Tropp 2008; Kulis et al. 2009; Chandrasekaran and Shah 2016].

**Tensor field processing.** Tensor-valued data are ubiquitous in various areas of imaging science, computer graphics and vision. In medical imaging, diffusion tensor imaging (DTI) [Wandell 2016] directly maps observed data to fields of tensors, and specific processing methods have been developed (see e.g. [Dryden et al. 2009; Deriche et al. 2006]. Tensor fields are also at the heart of anisotropic diffusions techniques in image processing [Weickert 1998], anisotropic meshing [Alliez et al. 2003; Demaret et al. 2006; Bougleux et al. 2009], anisotropic texture generation [Lagae et al. 2011], and find applications to line drawing [Vaxman et al. 2016] and data visualization [Hotz et al. 2004].

**OT on tensor fields.** The simplest way to define OT-like distances between arbitrary vector-valued measures is to use dual norms [Ning and Georgiou 2014], which correspond to generalizations of  $W_1$  OT for which transport cost equals ground distance. The corresponding metrics, however, have degenerate behavior in interpolation and barycenter problems (much like the  $L^1$  norm on functions) and only use the linear structure of matrices rather than their multiplicative structure. More satisfying notions of OT have recently been proposed in a dynamical (geodesic) way [Jiang et al. 2012; Carlen and Maas 2014; Chen et al. 2016]. A static formulation of a tensor-valued OT is proposed in [Ning et al. 2015], but it differs significantly from ours. It is initially motivated using a lifting that squares the number of variables, but a particular choice of cost reduces the computation to the optimization of a pair of couplings. In contrast, the formulation we propose in the present article is a direct generalization of unbalanced OT to matrices, which in turn enables the use of a Sinkhorn algorithm.

## 1.2 Contributions

We present a new static formulation of OT between tensor fields, which is the direct generalization of unbalanced OT from the scalar to the matrix case. Our second contribution is a fast entropic scaling algorithm generalizing the celebrated Sinkhorn iterative scheme. This leads to a method to compute geometrically-faithful interpolations between two tensor fields. Our third contribution is the extension of this approach to compute barycenters between several tensor fields. The Matlab code to reproduce the results of this article is available online.<sup>1</sup>

## 1.3 Notation

In the following, we denote  $\mathcal{S}^d \subset \mathbb{R}^{d \times d}$  the space of symmetric matrices,  $\mathcal{S}_+^d$  the closed convex cone of positive semidefinite matrices, and  $\mathcal{S}_{++}^d$  the open cone of positive definite matrices. We denote  $\exp : \mathcal{S}^d \rightarrow \mathcal{S}_{++}^d$  the matrix exponential, which is defined as  $\exp(P) = U \text{diag}_s(e^{\sigma_s})U^\top$  where  $P = U \text{diag}_s(\sigma_s)U^\top$  is an eigendecomposition of  $P$ . We denote  $\log : \mathcal{S}_{++}^d \rightarrow \mathcal{S}^d$  the matrix

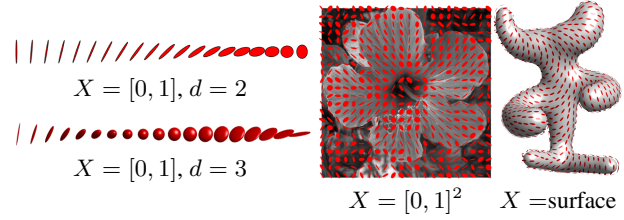


**Figure 2:** Displays of various types of tensor-valued measures  $\mu$ . The principal directions of an ellipse at some  $x_i \in X$  are the eigenvectors of  $\mu_i \in \mathcal{S}_+^d$ , while the principal width are given by its eigenvalues.

logarithm  $\log(P) = U \text{diag}_s(\log \sigma_s)U^\top$ , which is the inverse of  $\exp$  on  $\mathcal{S}_{++}^d$ .

A tensor-valued measure  $\mu$  defined on some space  $X$  is a vector-valued measure, where the “mass”  $\mu(A) \in \mathcal{S}_+^d$  associated to a measurable set  $A \subset X$  is a PSD matrix. In this article, in order to derive computational schemes, we focus on discrete measures. Such a measure  $\mu$  is a sum of Dirac masses  $\mu = \sum_{i \in I} \mu_i \delta_{x_i}$  where  $(x_i)_i \subset X$ , and  $(\mu_i)_i \in \mathcal{S}_+^d$  is a collection of PSD matrices. In this case,  $\mu(A) = \sum_{x_i \in A} \mu_i$ . Figure 2 shows graphically some examples of tensor-valued measures; we use this type of visualization through the article. In the following, since the sampling points  $(x_i)_i$  are assumed to be fixed and clear from the context, to ease readability, we do not make the distinction between the measure  $\mu$  and the collection of matrices  $(\mu_i)_i$ . This is an abuse of notation, but it is always clear from context whether we are referring to a measure or a collection of matrices.

The quantum entropy (also called von Neumann entropy) of a tensor-valued measure is

$$H(\mu) \stackrel{\text{def.}}{=} \sum_i H(\mu_i) \quad \text{where} \quad (1)$$

$$\forall P \in \mathcal{S}^d, \quad H(P) \stackrel{\text{def.}}{=} -\text{tr}(P \log(P) - P) - \iota_{\mathcal{S}_+^d}(P),$$

where  $\iota_C$  is the indicator function of a closed convex set  $C$ , i.e.  $\iota_C(P) = 0$  if  $P \in C$  and  $\iota_C(P) = +\infty$  otherwise. Note that  $H$  is a concave function. The quantum Kullback-Leibler divergence (also called quantum relative entropy) is the Bregman divergence associated to  $-H$ . For a collection of PSD matrices  $\mu = (\mu_i)_i, \xi = (\xi_i)_i$  in  $\mathcal{S}_+^d$  corresponding to measures defined on the same grid, assuming  $\xi_i \in \mathcal{S}_{++}^d$ , it is defined as

$$\text{KL}(\mu|\xi) \stackrel{\text{def.}}{=} \sum_i \text{KL}(\mu_i|\xi_i), \quad (2)$$

where for all  $(P, Q) \in \mathcal{S}_+^d \times \mathcal{S}_{++}^d$ , we denote

$$\text{KL}(P|Q) \stackrel{\text{def.}}{=} \text{tr}(P(\log(P) - \log(Q)) - P + Q) + \iota_{\mathcal{S}_{++}^d}(P)$$

which is convex with respect to both arguments. The inner product between collections of matrices  $\mu = (\mu_i)_i, \xi = (\xi_i)_i$  is

$$\langle \mu, \xi \rangle \stackrel{\text{def.}}{=} \sum_i \langle \mu_i, \xi_i \rangle \stackrel{\text{def.}}{=} \sum_i \text{tr}(\mu_i \xi_i^\top).$$

Given a collection of matrices  $\gamma = (\gamma_{i,j})_{i \in I, j \in J}$  the marginalization operators read

$$\gamma \mathbb{1}_J \stackrel{\text{def.}}{=} \left( \sum_j \gamma_{i,j} \right)_i \quad \text{and} \quad \gamma^\top \mathbb{1}_I \stackrel{\text{def.}}{=} \left( \sum_i \gamma_{i,j} \right)_j.$$

<sup>1</sup>Available as supplementary material.

## 2 Kantorovich Problem for Tensor-Valued Transport

We consider two measures that are sums of Dirac masses

$$\mu = \sum_{i \in I} \mu_i \delta_{x_i} \quad \text{and} \quad \nu = \sum_{j \in J} \nu_j \delta_{y_j} \quad (3)$$

where  $(x_i)_i \subset X$  and  $(y_j)_j \subset Y$ , and  $(\mu_i)_i \in \mathcal{S}_+^d$  and  $(\nu_j)_j \in \mathcal{S}_+^d$  are collections of PSD matrices. Our goal is to propose a new definition of OT between  $\mu$  and  $\nu$ .

### 2.1 Tensor Transportation

Following the initial static formulation of OT by Kantorovich [1942], we define a coupling  $\gamma = \sum_{i,j} \gamma_{i,j} \delta_{(x_i, y_j)}$  as a measure over the product  $X \times Y$  that encodes the transport of mass between  $\mu$  and  $\nu$ . In the matrix case,  $\gamma_{i,j} \in \mathcal{S}_+^d$  is now a PSD matrix, describing how much of mass is moved between  $\mu_i$  and  $\nu_j$ . Exact (balanced) transport would mean that the marginals  $(\gamma \mathbb{1}_J, \gamma^\top \mathbb{1}_I)$  must be equal to the input measures  $(\mu, \nu)$ . But as remarked by Ning et al. [2015], in contrast to the scalar case, in the matrix case (dimension  $d > 1$ ), this constraint is in general too strong, and there might exists no coupling satisfying these marginal constraints. We advocate in this work that the natural workaround for the matrix setting is the unbalanced case, and following [Liero et al. 2015], we propose to use a “relaxed” formulation where the discrepancy between the marginals  $(\gamma \mathbb{1}_J, \gamma^\top \mathbb{1}_I)$  and the input measures  $(\mu, \nu)$  is quantified according to some divergence between measures.

In the scalar case, the most natural divergence is the Kulback-Leibler divergence (which in particular gives rise to a natural Riemannian structure on positive measures, as defined in [Liero et al. 2016; Kondratyev et al. 2015; Chizat et al. 2016b]). We propose to make use of its quantum counterpart (2) via the following convex program

$$W(\mu, \nu) = \min_{\gamma} \langle \gamma, c \rangle + \rho_1 \text{KL}(\gamma \mathbb{1}_J | \mu) + \rho_2 \text{KL}(\gamma^\top \mathbb{1}_I | \nu) \quad (4)$$

subject to the constraint  $\forall (i, j), \gamma_{i,j} \in \mathcal{S}_+^d$ . Here  $\rho_1, \rho_2 > 0$  are constants balancing the “transport” effect versus the local modification of the matrices.

The matrix  $c_{i,j} \in \mathbb{R}^{d \times d}$  measures the cost of displacing an amount of (matrix) mass  $\gamma_{i,j}$  between  $x_i$  and  $y_j$  as  $\text{tr}(\gamma_{i,j} c_{i,j})$ . A typical cost, assuming  $X = Y$  is a metric space endowed with a distance  $d_X$ , is

$$c_{i,j} = d_X(x_i, y_j)^\alpha \text{Id}_{d \times d},$$

for some  $\alpha > 0$ . In this case, one should interpret the trace as the global mass of a tensor, and the total transportation cost is simply

$$\langle \gamma, c \rangle = \sum_{i,j} d_X(x_i, y_j)^\alpha \text{tr}(\gamma_{i,j}).$$

**Remark 1** (Classical OT). In the scalar case  $d = 1$ , (4) recovers exactly the log-entropic definition [Liero et al. 2015] of unbalanced optimal transport, which is studied numerically by Chizat et al. [2016a]. For isotropic tensors, i.e., all  $\mu_i$  and  $\nu_j$  are scalar multiples of the identity  $\text{Id}_{d \times d}$ , the computation also collapses to the scalar case (the  $\gamma_{i,j}$  are also isotropic). More generally, if all the  $(\mu_i, \nu_j)_{i,j}$  commute, they diagonalize in the same orthogonal basis, and (4) reduces to performing  $d$  independent unbalanced OT computations along each eigendirection.

**Remark 2** (Cost between single Dirac masses). When  $\mu = P\delta_x$  and  $\nu = Q\delta_x$  are two Dirac masses are the same location  $x$  and

associated to tensors  $(P, Q) \in (\mathcal{S}_+^d)^2$ , one obtains the following “metric” between tensors (assuming  $\rho_1 = \rho_2 = \rho$  for simplicity)

$$W(P\delta_x, Q\delta_x) = D(P, Q) \stackrel{\text{def.}}{=} \text{tr}(P + Q - 2\mathfrak{M}(P, Q))^{\frac{1}{2}} \quad (5)$$

where  $\mathfrak{M}(P, Q) \stackrel{\text{def.}}{=} \exp(\log(P)/2 + \log(Q)/2)$ . Unfortunately, in general  $D$  does not satisfy the triangle inequality. Note that when  $(P, Q)$  commute, one has  $D(P, Q) = \|\sqrt{P} - \sqrt{Q}\|$  which indeed satisfies the triangle inequality.

**Remark 3** (Quantum transport on curved geometries). If  $(\mu, \nu)$  are defined on a non-Euclidean space  $Y = X$ , like a smooth manifold, then formulation (4) should be handled with care, since it assumes all the tensors  $(\mu_i, \nu_j)_{i,j}$  are defined in some common basis. For smooth manifolds, the simplest workaround is to assume that these tensors are defined with respect to carefully selected orthogonal bases of the tangent planes, so that the field of bases is itself smooth. Unless the manifold is parallelizable, in particular if it has a trivial topology, it is not possible to obtain a globally smooth orthonormal basis; in general, any such field necessarily has a few singular points. In the following, we compute smoothly-varying orthogonal bases of the tangent planes following the method of Crane et al. [2010]. In this setting, the cost is usually chosen to be  $c_{i,j} = d_X(x_i, x_j)^\alpha \text{Id}_{d \times d}$  where  $d_X$  is the geodesic distance on  $X$ .

### 2.2 Quantum Transport Interpolation

Given two input measures  $(\mu, \nu)$ , we denote  $\gamma$  as a solution of (4) or, in practice, its regularized version (see (7) below). The coupling  $\gamma$  defines a (fuzzy) correspondence between the tensor fields. A typical use of this correspondence is to compute a continuous interpolation between these fields. Section 3.3 shows some numerical illustrations of this interpolation. Note also that Section 4 proposes a generalization of this idea to compute an interpolation (barycenter) between more than two input fields.

Mimicking the definition of the optimal transport interpolation (the so-called McCann displacement interpolation; see for instance [Santambrogio 2015]), we propose to use  $\gamma$  to define a path  $t \in [0, 1] \mapsto \mu_t$  interpolating between  $(\mu, \nu)$ . For simplicity, we assume the cost has the form  $c_{i,j} = d_X(x_i, y_j)^\alpha \text{Id}_{d \times d}$  for some ground metric  $d_X$  on  $X = Y$ . We also suppose we can compute efficiently the interpolation between two points  $(x_i, y_j) \in X^2$  as

$$x_{i,j}^t \stackrel{\text{def.}}{=} \underset{x \in X}{\text{argmin}} (1-t)d_X^2(x_i, x) + td_X^2(y_j, x).$$

For instance, over Euclidean spaces,  $g_t$  is simply a linear interpolation, and over more general manifold, it is a geodesic segment. We also denote

$$\bar{\mu}_i \stackrel{\text{def.}}{=} \mu_i \left( \sum_j \gamma_{i,j} \right)^{-1} \quad \text{and} \quad \bar{\nu}_j \stackrel{\text{def.}}{=} \nu_j \left( \sum_i \gamma_{i,j} \right)^{-1}$$

the adjustment factors which account for the imperfect match of the marginal associated to a solution of (7); the adjusted coupling is

$$\gamma_{i,j}^t \stackrel{\text{def.}}{=} [(1-t)\bar{\mu}_i + t\bar{\nu}_j]\gamma_{i,j}.$$

Finally, the interpolating measure is then defined as

$$\forall t \in [0, 1], \quad \mu_t \stackrel{\text{def.}}{=} \sum_{i,j} \gamma_{i,j}^t \delta_{x_{i,j}^t}. \quad (6)$$

One easily verifies that this measure indeed interpolates the two input measures, i.e.  $(\mu_{t=0}, \mu_{t=1}) = (\mu, \nu)$ . This formula (6) generates the interpolation by creating a Dirac tensor  $\gamma_{i,j}^t \delta_{x_{i,j}^t}$  for each coupling entry  $\gamma_{i,j}$ , and this tensor travels between  $\mu_i \delta_{x_i}$  (at  $t = 0$ ) and  $\nu_j \delta_{y_j}$  (at  $t = 1$ ).

246 247 248 249 250 251 252 253 254 255 256 257 258 259 260 261 262 263 264 265 266 267 268 269 270 271 272 273 274 275 276 277 278 279 280 281 282 283 284 285 286 287 288 289 290 291 292 293 294 295 296 297 298 299 300 301 302 303 304 305 306 307 308 309 310 311 312 313 314 315 316 317 318 319 320 321 322 323

**Remark 4** (Computational cost). We observed numerically that, similarly to the scalar case, the optimal coupling  $\gamma$  is sparse, meaning that only of the order of  $O(|I|)$  non-zero terms are involved in the interpolating measure (6). Note that the entropic regularization algorithm detailed in Section 3 destroys this exact sparsity, but we found numerically that that thresholding to zero the small entries of  $\gamma$  generates accurate approximations.

### 3 Quantum Sinkhorn

254 The convex program (4) defining quantum OT is computationally 255 challenging because it can be very large scale (problem size is 256  $|I| \times |J|$ ) for imaging applications, and it involves matrix exponential 257 and logarithm. In this section, leveraging recent advances in 258 computational OT initiated by Cuturi [2013], we propose to use a 259 similar entropy regularized strategy (see also section 1), but this time 260 with the quantum entropy (1).

#### 3.1 Entropic Regularization

261 We define an entropic regularized version of (4)

$$W_\varepsilon(\mu, \nu) \stackrel{\text{def.}}{=} \min_{\gamma} \langle \gamma, c \rangle + \rho_1 \text{KL}(\gamma \mathbb{1}_J | \mu) + \rho_2 \text{KL}(\gamma^\top \mathbb{1}_I | \nu) - \varepsilon H(\gamma). \quad (7)$$

263 Note that when  $\varepsilon = 0$ , one recovers the original problem (4). This 264 is a strongly convex program, with a unique solution. The crux of 265 this approach, as already known in the scalar case (see [Chizat et al. 266 2016a]), is that its convex dual has a particularly simple structure, 267 which is amenable to a simple alternating maximization strategy.

**Proposition 1.** *The dual problem associated to (7) reads*

$$\begin{aligned} W_\varepsilon(\mu, \nu) = \max_{u, v} & -\text{tr} \left[ \rho_1 \sum_i (e^{u_i + \log(\mu_i)} - \mu_i) \right. \\ & \left. + \rho_2 \sum_j (e^{v_j + \log(\nu_j)} - \nu_j) + \varepsilon \sum_{i,j} e^{\mathcal{K}(u, v)_{i,j}} \right], \end{aligned} \quad (8)$$

269 where  $u = (u_i)_{i \in I}, v = (v_j)_{j \in J}$  are collection of symmetric (not 270 necessarily positive) matrices  $u_i, v_j \in \mathcal{S}^d$ , where we define

$$\mathcal{K}(u, v)_{i,j} \stackrel{\text{def.}}{=} -\frac{c_{i,j} + \rho_1 u_i + \rho_2 v_j}{\varepsilon}. \quad (9)$$

271 Furthermore, the following primal-dual relationships hold at optimality:

$$\forall (i, j), \quad \gamma_{i,j} = \exp(\mathcal{K}(u, v)_{i,j}). \quad (10)$$

273 274 *Proof.* Applying the Fenchel–Rockafellar duality theorem [Rockafellar 1970] to (7) leads to the dual program

$$\max_{u, v} -\varepsilon \text{KL}^*(\mathcal{K}_0(u, v) | \xi) - \rho_1 \text{KL}^*(u | \mu) - \rho_2 \text{KL}^*(v | \nu) - \varepsilon \text{tr}(\xi),$$

275 where here  $\text{KL}^*(\cdot | \mu)$  corresponds to the Legendre transform with 276 respect to the first argument of the KL divergence,  $\mathcal{K}_0(u, v)_{i,j} \stackrel{\text{def.}}{=} -\frac{\rho_1 u_i + \rho_2 v_j}{\varepsilon}$  and  $\xi_{i,j} \stackrel{\text{def.}}{=} \exp(-c_{i,j}/\varepsilon)$  for all  $i, j$ . The following 277 Legendre formula leads to the desired result:

$$\text{KL}^*(u | \mu) = \sum_i \text{tr}(\exp(u_i + \log(\mu_i)) - \mu_i).$$

### 3.2 Quantum Sinkhorn Algorithm

281 It is possible to use Dykstra's algorithm [1983] (see [Bauschke and 282 Lewis 2000] for its extension to Bregman divergences) to solve (8). 283 This corresponds to alternatively maximizing (8) with respect to  $u$  and 284  $v$ . The following proposition states that the maximization with 285 respect to either  $u$  or  $v$  leads to two fixed-point equations. These 286 fixed points are conveniently written using the log-sum-exp operator, 287

$$\text{LSE}_j(K_{i,j}) \stackrel{\text{def.}}{=} \log \sum_j \exp(K_{i,j}), \quad (11)$$

288 where the sum on  $j$  is replaced by a sum on  $i$  for  $\text{LSE}_i$ .

**Proposition 2.** *For  $v$  fixed (resp.  $u$  fixed), the minimizer  $u$  (resp.  $v$ ) of (8) satisfies*

$$\forall i, \quad u_i = \text{LSE}_j(\mathcal{K}(u, v)_{i,j}) - \log(\mu_i), \quad (12)$$

$$\forall j, \quad v_j = \text{LSE}_i(\mathcal{K}(u, v)_{i,j}) - \log(\nu_j), \quad (13)$$

291 where  $\mathcal{K}(u, v)$  is defined in (9).

292 293 *Proof.* Writing the first order condition of (8) with respect to each  $u_i$  leads to

$$\rho_1 e^{u_i + \log(\mu_i)} - \rho_1 \sum_j e^{\mathcal{K}(u, v)_{i,j}} = 0$$

294 295 which gives the desired expression. A similar expression holds for the first order conditions with respect to  $v_j$ .  $\square$

296 297 298 299 300 A simple fixed point algorithm is then obtained by replacing in 296 Dykstra's the explicit alternating minimization with respect to  $u$  and 297  $v$  by just one step of fixed point iterations (12) and (13). To make 298 the resulting fixed point contractant and ensure linear convergence, 299 one introduces relaxation parameters  $(\tau_1, \tau_2)$ .

300 The quantum Sinkhorn algorithm is detailed in Algorithm 1. It 301 alternates between the updates of  $u$  and  $v$ , using relaxed fixed point 302 iterations associated to (12) and (13). We use the following  $\tau$ -relaxed 303 assignment notation

$$a \xleftarrow{\tau} b \quad \text{means that} \quad a \leftarrow (1 - \tau)a + \tau b. \quad (14)$$

305 The algorithm outputs the scaled kernel  $\gamma_{i,j} = \exp(K_{i,j})$ .

306 307 308 309 310 311 *Remark 5* (Choice of  $\tau_k$ ). In the scalar case, i.e.  $d = 1$  (and also for isotropic input tensors), when using  $\tau_k = \frac{\varepsilon}{\rho_k + \varepsilon}$  for  $k = 1, 2$ , one retrieves exactly Sinkhorn iterations for unbalanced transport as described in [Chizat et al. 2016a], and each update of  $u$  (resp.  $v$ ) exactly solves the fixed point (12) (resp. (13)). Moreover, it is simple to check that these iterates are contractant whenever

$$\tau_k \in ]0, \frac{2\varepsilon}{\varepsilon + \rho_k}[ \quad \text{for } k = 1, 2.$$

312 313 314 315 316 317 and this property has been observed experimentally for higher dimensions  $d = 2, 3$ . Using higher values for  $\tau_k$  actually often improves the (linear) convergence rate. Figure 3 displays a typical example of convergence, and exemplifies the usefulness of using large values of  $\tau_k$ , which leads to a speed-up of a factor 6 with respect to the usual Sinkhorn's choice  $\tau_k = \frac{\varepsilon}{\varepsilon + \rho_k}$ .

318 319 320 321 322 323 *Remark 6* (Stability). In contrast to the usual implementation of Sinkhorn's algorithm, which is numerically unstable for small  $\varepsilon$  because it requires to compute  $e^{u/\varepsilon}$  and  $e^{v/\varepsilon}$ , the proposed iterations using the LSE operator are stable. The algorithm can thus be run for arbitrary small  $\varepsilon$ , although the linear speed of convergence is of course impacted.

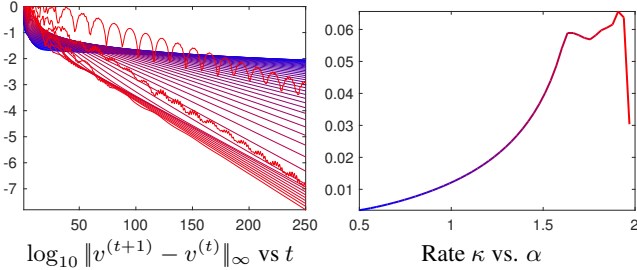


**Figure 3:** Display of convergence of Sinkhorn Algorithm 1 for the example displayed on the first row of Figure 1. Denoting  $u^{(t)}$  the value of the variable  $u$  at iteration  $t$ , the left plot shows the fixed point residual error for increasing values of  $\tau_1 = \tau_2 = \frac{\alpha\varepsilon}{\varepsilon+\rho}$  with  $\alpha \in [0.5, 2]$  (blue to red). The algorithm exhibits a linear convergence rate,  $\log_{10} \|v^{(t+1)} - v^{(t)}\|_\infty \sim -\kappa t$  for some  $\kappa > 0$ , and the right plot displays  $\kappa$  as a function of  $\alpha$ .

```

function QUANTUM-SINKHORN( $\mu, \nu, c, \varepsilon, \rho_1, \rho_2$ )
   $\forall k = 1, 2, \dots, \lceil \frac{2\varepsilon}{\varepsilon+\rho_k} \rceil$ ,
   $\forall (i, j) \in I \times J, (u_i, v_j) \leftarrow (0_{d \times d}, 0_{d \times d})$ 
  for  $s = 1, 2, 3, \dots$ 
     $K \leftarrow \mathcal{K}(u, v)$ 
     $\forall i \in I, u_i \leftarrow \text{LSE}_j(K_{i,j}) - \log(\mu_i)$ 
     $K \leftarrow \mathcal{K}(u, v)$ 
     $\forall j \in J, v_j \leftarrow \text{LSE}_i(K_{i,j}) - \log(\nu_j)$ 
  return  $(\gamma_{i,j} = \exp(K_{i,j}))_{i,j}$ 

```

**Algorithm 1:** Quantum-Sinkhorn iterations to compute the optimal coupling  $\gamma$  of the regularized transportation problem (7). The operator  $\mathcal{K}$  is defined in (9).

**Remark 7** (log and exp computations). A major computational workload of the Q-Sinkhorn Algorithm 1 is the repetitive computation of matrix exp and log. For  $d \in \{2, 3\}$  it is possible to use closed form expressions to diagonalize the tensors, so that the overall complexity is comparable with the usual scalar case  $d = 1$ . While the applications Section 5 only considers these low-dimensional settings, high dimensional problems are of interest, typically for machine learning applications. In these cases, one has to resort to iterative procedures, such as rapidly converging squaring schemes [Al-Mohy and Higham 2009; Al-Mohy and Higham 2012].

**Remark 8** (Computational complexity). For low-dimensional problems (typically for those considered in Section 5), the Q-Sinkhorn Algorithm 1 scales to grid sizes of roughly 6k points (with machine-precision solutions computed in a few minutes on a standard laptop). For large scale grids, even storing the full coupling  $\gamma$  becomes prohibitive. We however observed numerically that, similarly to the usual scalar case, the optimal  $\gamma$  solving (7) is highly sparse (up to machine precision for small enough  $\varepsilon$ ). We thus found that using the multi-scale refinement strategy introduced in [Schmitzer 2016] is able to make the Q-Sinkhorn scales to high resolution grids. It is not used to produce the figures of this article, but it is available in the companion computational toolbox.

### 3.3 Numerical Illustrations

Figures 1 and 4 illustrates on synthetic examples of input tensor fields  $(\mu, \nu)$  our interpolation method. We recall that it is obtained in two steps:

- One first computes the optimal  $\gamma$  solving (7) using Sinkhorn

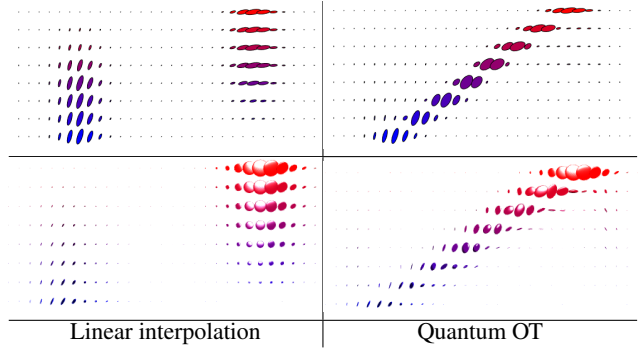


**Figure 4:** Comparison of linear and quantum-OT interpolation (using formula (6)). Each row shows a field of tensors (top  $d = 2$ , bottom  $d = 3$ ) along a linear segment from  $t = 0$  to  $t = 1$  ( $t$  axis is vertical).

iterations (Algorithm 1).

- Then, for any  $t \in [0, 1]$ , one computes  $\mu_t$  using this optimal  $\gamma$  with formula (6).

Figure 4 shows examples of interpolations on a 1-D domain  $X = Y = [0, 1]$  with tensors of dimension  $d = 2$  and  $d = 3$ , and a ground cost  $c_{i,j} = |x_i - y_j|^2 \text{Id}_{d \times d}$ . It compares the OT interpolation, which achieves a “mass displacement,” to the usual linear interpolation  $(1-t)\mu + t\nu$ , which only performs a pointwise interpolation of the tensors.

Figure 1 shows larger scale examples. The first row corresponds to  $X = Y = [0, 1]^2$  and  $d = 2$ , with cost  $c_{i,j} = \|x_i - y_j\|^2 \text{Id}_{2 \times 2}$ , which is a typical setup for image processing. The second row corresponds to  $X = Y$  being a triangulated mesh of a surface, and the cost is proportional to the squared geodesic distance  $c_{i,j} = d_X(x_i, y_j)^2 \text{Id}_{2 \times 2}$ .

## 4 Quantum Barycenters

Following Aguech and Carlier [2011] (see also [Benamou et al. 2015; Solomon et al. 2015] for numerical methods using entropic regularization), we now propose a generalization of the OT problem (4), where, instead of coupling only two input measures, one tries to couple an arbitrary set of inputs, and compute their Fréchet means.

### 4.1 Barycenter Optimization Problem

Given some input measures  $(\mu^\ell)_\ell$ , the quantum barycenter problem reads

$$\min_{\nu} \sum_{\ell} w_{\ell} W_{\varepsilon}(\mu^{\ell}, \nu), \quad (15)$$

where  $(w_{\ell})_{\ell}$  is a set of positive weights normalized so that  $\sum_{\ell} w_{\ell} = 1$ . In the following, for simplicity, we set

$$\rho_1 = \rho \quad \text{and} \quad \rho_2 = +\infty$$

in the definition (4) of  $W_{\varepsilon}$ . Note that the choice  $\rho_2 = +\infty$  corresponds to imposing the exact hard marginal constraint  $\gamma^{\top} \mathbb{1}_J = \nu$ . **Remark 9** (Barycenters between single Dirac masses). If all the input measures are concentrated on single Diracs  $\mu^{\ell} = P_{\ell} \delta_{x_{\ell}}$ , then the single Dirac barycenter (unregularized, i.e.,  $\varepsilon = 0$ ) for a cost  $d_X(x, y)^{\alpha} \text{Id}_{d \times d}$  is  $P \delta_x^*$  where  $x^* \in X$  is the usual barycenter for the distance  $d_X$ , solving

$$x^* \in \operatorname{argmin}_x \mathcal{E}(x) = \sum_{\ell} w_{\ell} d_X^{\alpha}(x_{\ell}, x)$$

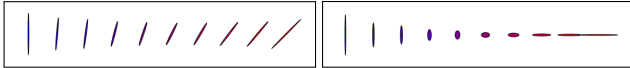


**Figure 5:** Two examples of pointwise (without transportation) interpolations, using formula (16). Here  $P_1$  and  $P_2$  are represented using the blue/red ellipses on the left/right, and weights are  $(w_1, w_2) = (1 - t, t)$  for  $t \in [0, 1]$  from left to right.

```

function QUANTUM-BARYCENTER( $(\mu_\ell)_{\ell=1}^L, c, \varepsilon, \rho$ )
    Choose  $\tau_1 \in ]0, \frac{2\varepsilon}{\varepsilon+\rho}[$ ,  $\tau_2 \in ]0, 2[$ .
     $\forall (i, j) \in I \times J, (u_i, v_j) \leftarrow (0_{d \times d}, 0_{d \times d})$ 
    for  $s = 1, 2, 3, \dots$ 
        for  $\ell = 1, \dots, L$ 
             $K^\ell \leftarrow \mathcal{K}(u^\ell, v^\ell),$ 
             $\forall i \in I, u_i^\ell \xleftarrow{\tau_1} \text{LSE}_j(K_{i,j}^\ell) - \log(\mu_i^\ell),$ 
             $K^\ell \leftarrow \mathcal{K}(u^\ell, v^\ell).$ 
         $\forall j \in J, \log(\nu_j) \leftarrow \sum_\ell w_\ell (\text{LSE}_i(K_{i,j}^\ell) + v_j^\ell / \varepsilon).$ 
        for  $\ell = 1, \dots, L$ 
             $\forall j \in J, v_j^\ell \xleftarrow{\tau_2} \varepsilon \text{LSE}_i(K_{i,j}^\ell) + v_j^\ell - \varepsilon \log(\nu_j).$ 
    return  $\nu$ 

```

**Algorithm 2:** Quantum-Barycenter iterations to compute the optimal barycenter measure  $\nu$  solving (15). The operator  $\mathcal{K}$  is defined in (18).

and the barycentric matrix is

$$P = e^{-\frac{\varepsilon(x^*)}{\rho}} \exp \left( \sum_\ell w_\ell \log(P_\ell) \right). \quad (16)$$

Figure 5 illustrates the effect of a pointwise interpolation (i.e. at the same location  $x_\ell$  for all  $\ell$ ) between tensors.

Problem (15) is convex, and similarly to (8), it can be rewritten in dual form.

**Proposition 3.** The optimal  $\nu$  solving (15) is solution of

$$\begin{aligned} \max_{(u^\ell, v^\ell)} \min_{\nu} & - \sum_\ell w_\ell \text{tr} \left[ \rho \sum_i e^{u_i^\ell + \log(\mu_i^\ell)} \right. \\ & \left. + \sum_j \nu_j v_j^\ell + \varepsilon \sum_{i,j} e^{\mathcal{K}(u^\ell, v^\ell)_{i,j}} \right], \end{aligned} \quad (17)$$

where here we define  $\mathcal{K}$  as

$$\mathcal{K}(u, v)_{i,j} \stackrel{\text{def.}}{=} -\frac{c_{i,j} + \rho u_i + v_j}{\varepsilon}. \quad (18)$$

## 4.2 Quantum Barycenter Sinkhorn

Similarly to Proposition 2, the dual solutions of (17) satisfy a set of coupled fixed point equations:

**Proposition 4.** Optimal  $(u^\ell, v^\ell)_\ell$  for (17) satisfy

$$\forall (i, \ell), \text{LSE}_j(\mathcal{K}(u^\ell, v^\ell)_{i,j}) - \log(\mu_i^\ell) = u_i^\ell \quad (19)$$

$$\forall (j, \ell), \text{LSE}_i(\mathcal{K}(u^\ell, v^\ell)_{i,j}) = \log(\nu_j) \quad (20)$$

$$\sum_\ell w_\ell v^\ell = 0. \quad (21)$$

*Proof.* The proof of (19) and (20) is the same as the one of Proposition 2. Minimization of (17) on  $\nu$  leads to (21).  $\square$

The extension of the quantum Sinkhorn algorithm to solve the barycenter problem (2) is detailed in Algorithm 2. It alternates between the updates of  $u$ ,  $\nu$  and  $v$ , using the relaxed version of the fixed point equations (19), (20) and (21). The notation  $\xleftarrow{\tau}$  refers to a relaxed assignment as defined in (14).

**Remark 10** (Choice of  $\tau$ ). Remark 5 also applies for this Sinkhorn-like scheme, and setting  $(\tau_1, \tau_2) = (\frac{\varepsilon}{\rho+\varepsilon}, 1)$  leads, in the scalar case  $d = 1$ , to the algorithm in [Chizat et al. 2016a]. We found experimentally that this choice leads to contracting (and hence linearly converging) iterations, and that higher values of  $\tau$  usually accelerate the convergence rate.

**Remark 11** (Scalar and isotropic cases). Note that in the scalar case  $d = 1$  and for isotropic input tensors (multiples of the identity), one retrieves the provably convergent unbalanced barycenter algorithm in [Chizat et al. 2016a].

## 4.3 Numerical Illustrations

Figure 6 shows examples of barycenters  $\nu$  solving (15) between four input measures  $(\mu^\ell)_{\ell=1}^4$ . The horizontal/vertical axes of the figures are indexed by  $(t_1, t_2) \in [0, 1]^2$  (on a  $5 \times 5$  grids) and parameterize the weights  $(w_\ell)_{\ell=1}^4$  appearing in (15) as

$$(w_1, w_2, w_3, w_4) \stackrel{\text{def.}}{=} ((1-t_1)(1-t_2), (1-t_1)t_2, t_1(1-t_2), t_1, t_2). \quad (22)$$

The left part of Figure 6 corresponds to measures on  $X = Y = [0, 1]^2$  with  $d = 2$  and ground cost  $c_{i,j} = \|x_i - x_j\|^2 \text{Id}_{2 \times 2}$ . The right part of Figure 6 corresponds to measures on  $X = Y$  being a surface mesh with  $d = 2$  (the tensors are defined on the tangent planes) and a ground cost is  $c_{i,j} = d_X(x_i, x_j)^2 \text{Id}_{2 \times 2}$  where  $d_X$  is the geodesic distance on the mesh.

## 5 Applications

This section showcases four different applications of Q-OT to register and interpolate tensor fields. Unless otherwise stated, the data is normalized to the unit cube  $[0, 1]^d$  (here  $d = 2$  for images) and discretized on grids of  $|I| = |J| = 60^d$  points. The regularization parameter is set to  $\varepsilon = 0.08^2$ , the fidelity penalty to  $\rho = 1$ , and the relaxation parameter for Sinkhorn to  $\tau_k = \frac{1.8\varepsilon}{\varepsilon + \rho_k}$ .

### 5.1 Anisotropic Space-Varying Procedural Noise

Texture synthesis using procedural noise functions is widely used in rendering pipelines and video games because of both its low storage cost and the fact that it is typically parameterized by a few meaningful parameters [Lagae et al. 2010]. Following Lagae et al. [2011] we consider here a spatially-varying Gabor noise function (i.e. non-stationary Gaussian noise), whose covariance function is parameterized using a PSD-valued field  $\mu$ . Quantum optimal transport allows to interpolate and navigate between these noise functions by transporting the corresponding tensor fields. The initial Gabor noise method makes use of sparse Gabor splattering [Lagae et al. 2010] (which enables synthesis at arbitrary resolution and zooming). For simplicity, we rather consider here a more straightforward method, where the texture  $f_{t_0}$  is obtained by stopping at time  $t = t_0$  an anisotropic diffusion guided by the tensor field  $\mu$  of a high frequency noise  $\mathcal{N}$  (numerically a white noise on a grid)

$$\frac{\partial_t f_t}{\partial t} = \text{div}(\mu \nabla f_t), \quad \text{where } f_{t=0} \sim \mathcal{N},$$

where  $(\mu \nabla f_t)(x) \stackrel{\text{def.}}{=} \mu(x)(\nabla f_t(x))$  is the vector field obtained by applying the tensor  $\mu(x) \in \mathcal{S}_2^+$  to the gradient vector  $\nabla f_t(x) \in \mathbb{R}^2$ . Locally around  $x$ , the texture is stretched in the direction of the

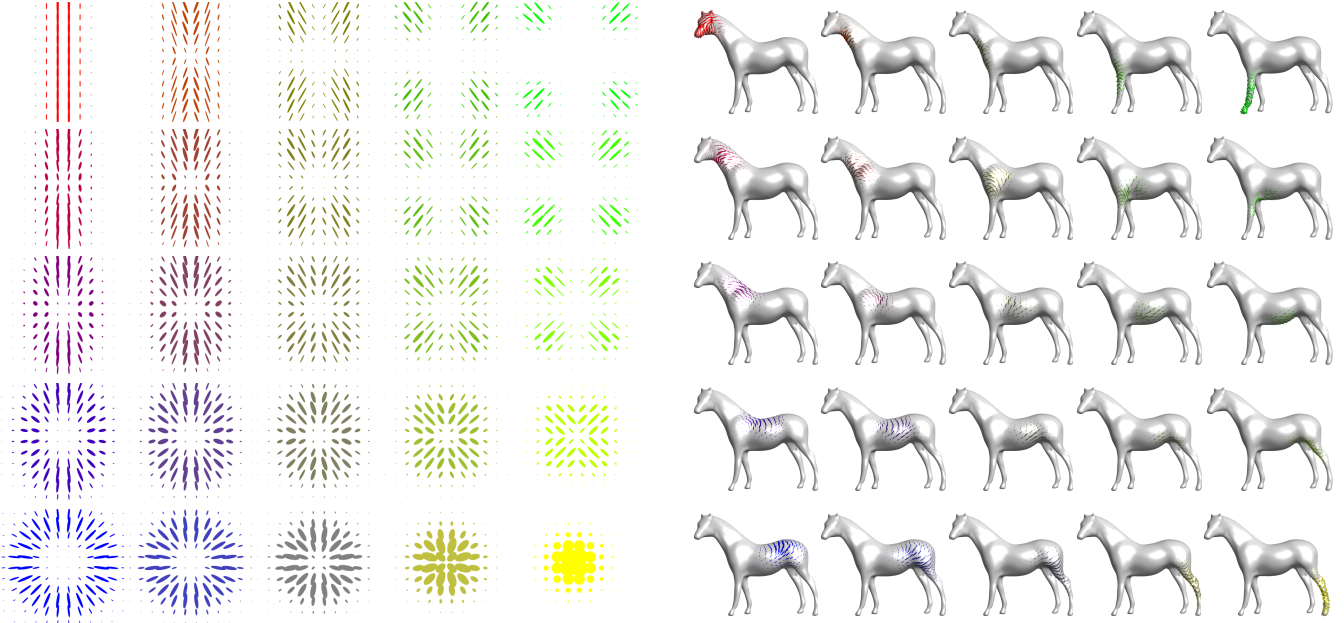


**Figure 6:**  $5 \times 5$  barycenters of four input measures (displayed in the four corners). The weights  $w \in \mathbb{R}^4$  correspond to bilinear interpolation weights (22) inside the square.

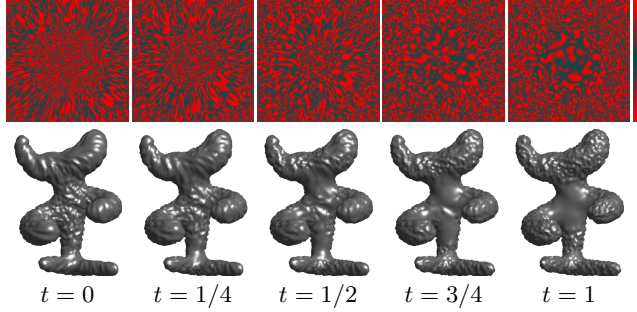


**Figure 7:** Example of interpolation between two input procedural anisotropic noise functions. The PSD tensor field parameterizing the texture are displayed on Figure 1. The colormap used to render the anisotropic texture is displayed on the last column.

449 main eigenvector of  $\mu(x)$ , highly anisotropic tensor giving rise to  
450 elongated “stripes” as opposed to isotropic tensor generating “spots.”

451 Numerically,  $f$  is discretized on a 2-D grid, and  $\mu$  is represented on  
452 this grid as a sum of Dirac masses (3). On Euclidian domains  $X$ ,  $\nabla$   
453 and  $\text{div}$  are computed using finite differences, while on triangulated  
454 mesh, they are implemented using standard piecewise-linear finite  
455 element primitives. Figure 7 shows two illustrations of this method.  
456 The top row generates an animated color texture by indexing a non-  
457 linear black-red colormap (displayed on the right) using  $f_t$ . Bottom  
458 row generates an animated bump-mapped surface using  $f_t$  to offset  
459 the mesh surface in the normal direction.

## 460 5.2 Anisotropic Meshing

461 Approximation with anisotropic piecewise linear finite elements  
462 on a triangulated mesh is a fundamental tool to address tasks such  
463 as discretizing partial differential equations, performing surface  
464 remeshing [Alliez et al. 2003] and image compression [Demaret

465 et al. 2006]. A common practice is to generate triangulations  
466 complying with a PSD tensor sizing field  $\mu$ , i.e. such that a tri-  
467 angle centered at  $x \in X$  should be inscribed in the ellipsoid  
468  $\{u \in X ; (u - x)^\top \mu(x)(u - x) \leq \delta\}$  for some  $\delta$  controlling the  
469 triangulation density. A well-known result is that, to locally approx-  
470 imate a smooth convex  $C^2$  function  $f$ , the optimal shapes of triangles  
471 is dictated by the Hessian  $Hf$  of the function (see [Shewchuk 2002]).  
472 In practice, people use  $\mu(x) = |Hf(x)|^\alpha$  for some exponent  $\alpha > 0$   
473 (which is related to the quality measure of the approximation), where  
474  $|\cdot|^\alpha$  indicates the spectral application of the exponentiation (as for  
475 matrix exp or log).

476 Figure (8) shows that Q-OT can be used (using formula (6)) to inter-  
477 polate between two sizing fields  $(\mu, \nu)$ , which are computed from the  
478 Hessians (with here  $\alpha = 1$ ) of two initial input images  $(f, g)$ . The  
479 resulting anisotropic triangulations are defined as geodesic Delau-  
480 nay triangulations for the Riemannian metric defined by the tensor  
481 field, and are computed using the method detailed in [Bougleux  
482 et al. 2009]. This interpolation could typically be used to track the  
483 evolution of the solution of some PDE.

## 484 5.3 Diffusion Tensor Imaging

485 Diffusion tensor magnetic resonance imaging (DTI) is a popular  
486 technique to image the white matter of the brain (see [Wandell  
487 2016] for a recent overview). DTI measures the diffusion of water  
488 molecules, which can be compactly encoded using a PSD tensor  
489 field  $\mu(x) \in \mathcal{S}_+^3$ , whose anisotropy and size matches the local  
490 diffusivity. A typical goal of this imaging technique is to map  
491 the brain anatomical connectivity, and in particular track the white  
492 matter fibers. This requires a careful handling of the tensor’s energy  
493 (its trace) and anisotropy, so that using Q-OT is a perfect fit for such  
494 data.

495 Figure 9 shows an application of Q-OT for the interpolation (using 6)  
496 between 2-D slices from DTI tensor fields  $(\mu, \nu)$  acquired on two  
497 different subjects. This data is extracted from the studies [Pestilli  
498 et al. 2014; Takemura et al. 2016]. These two patients exhibit differ-

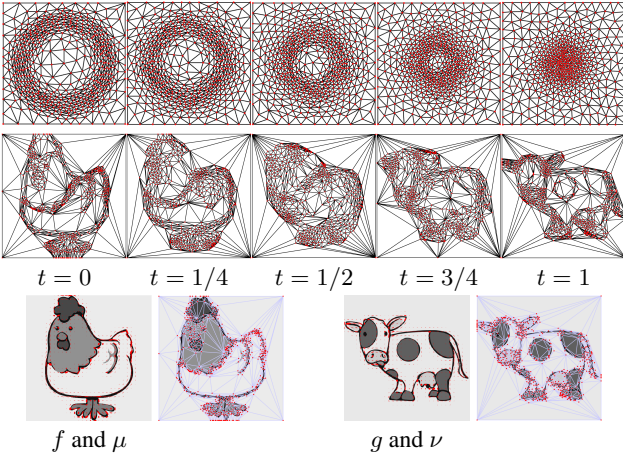


**Figure 8:** Two examples of interpolation between two input sizing fields  $(\mu_{t=0}, \mu_{t=1}) = (\mu, \nu)$ . **First row:** triangulation evolution for the sizing fields displayed on Figure 1. **Second row:** the input sizing fields  $(\mu_{t=0}, \mu_{t=1}) = (\mu, \nu)$  are displayed on the third row, and are defined using the absolute value ( $\alpha = 1$ ) of the Hessian of the underlying images ( $f, g$ ).

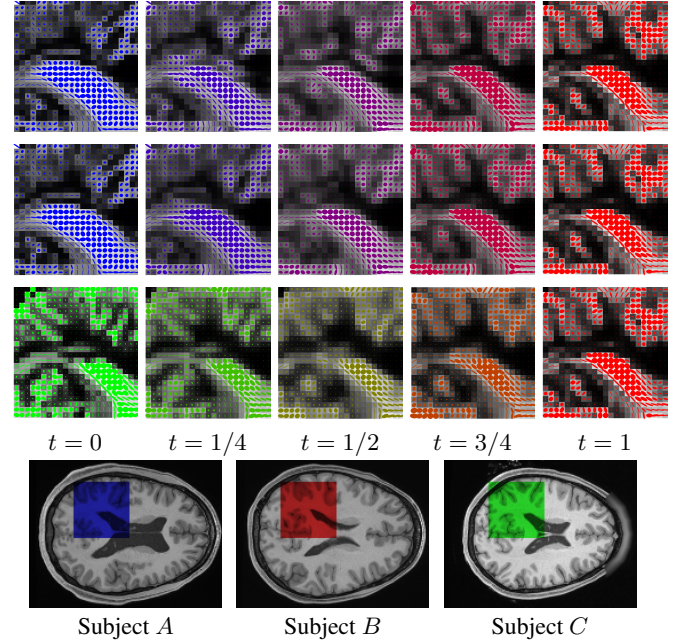


**Figure 9:** Interpolation between two 2-D slices of 3-D DTI tensor fields  $(\mu, \nu) = (\mu_{t=0}, \mu_{t=1})$ . For readability, only the X/Y components of the tensors are displayed. **First row:** interpolation between subjects (A, B) obtained using  $\rho = 1$ . **Second row:** interpolation between subjects (A, B) obtained using  $\rho = 0.05$ . **Third row:** interpolation between subjects (C, B) obtained using  $\rho = 0.05$ . **Fourth row:** anatomical MRI images of subjects (A, B, C) indicating the region of interest where the computations are performed.

ent anatomical connectivity geometries, and Q-OT is able to track the variation in both orientation and magnitude of the diffusion tensors. This figure also compares the different data fidelity parameters  $\rho \in \{0.05, 1\}$ . Selecting  $\rho = 1$  enforces an overly-strong conservation constraint and leads to interpolation artifacts (in particular some structure are split during the interpolation). In contrast, selecting  $\rho = 0.05$  introduces enough mass creation/destruction during the interpolation to be able to cope with strong inter-subject variability.

499  
500  
501  
502  
503  
504  
505  
506  
507  
508  
509  
510  
511  
512  
513  
514  
515  
516  
517  
518  
519  
520  
521  
522  
523  
524  
525  
526  
527  
528  
529  
530  
531  
532  
533  
534  
535  
536  
537  
538  
539  
540  
541  
542  
543  
544  
545  
546  
547  
548  
549  
550  
551

ent anatomical connectivity geometries, and Q-OT is able to track the variation in both orientation and magnitude of the diffusion tensors. This figure also compares the different data fidelity parameters  $\rho \in \{0.05, 1\}$ . Selecting  $\rho = 1$  enforces an overly-strong conservation constraint and leads to interpolation artifacts (in particular some structure are split during the interpolation). In contrast, selecting  $\rho = 0.05$  introduces enough mass creation/destruction during the interpolation to be able to cope with strong inter-subject variability.

#### 5.4 Spectral Color Texture Synthesis

As advocated initially in [Galerne et al. 2011], a specific class of textured images (so-called micro-textures) is well-modeled using stationary Gaussian fields. In the following, we denote  $p$  the pixel positions and  $x$  the Fourier frequency indices. For color images, these fields are fully characterized by their mean  $m \in \mathbb{R}^3$  and their Fourier power spectrum, which is a tensor valued field  $\mu(x)$  where, for each frequency  $x$  (defined on a 2-D grid)  $\mu(x) \in \mathbb{C}^{3 \times 3}$  is a complex positive semi-definite hermitian matrix.

In practice,  $\mu(x)$  is estimated from an exemplar color image  $f(p) \in \mathbb{R}^3$  using an empirical spectrogram

$$\mu(x) \stackrel{\text{def.}}{=} \frac{1}{K} \sum_{k=1}^K \hat{f}_k(x) \hat{f}_k(x)^* \in \mathbb{C}^{3 \times 3} \quad (23)$$

where  $\hat{f}_k$  is the Fourier transform of  $f_k(p) \stackrel{\text{def.}}{=} f(p)w_k(p)$  (computed using the FFT),  $w_k$  are windowing functions centred around  $K$  locations in the image plane, and  $v^* \in \mathbb{C}^{1 \times 3}$  denoted the transpose-conjugate of a vector  $v \in \mathbb{C}^{3 \times 1}$ . Increasing the number  $K$  of windowed estimations helps to avoid having rank-deficient covariances ( $K = 1$  leads to a field  $\mu$  of rank-1 tensors).

Randomized new textures are then created by generating random samples  $F(p) \in \mathbb{R}^3$  from the Gaussian field, which is achieved by defining the Fourier transform  $\hat{F}(x) \stackrel{\text{def.}}{=} m + \hat{N}(x)\sqrt{\mu(x)}\mathbb{1}_3$ , where  $N(p)$  is the realization of a Gaussian white noise, and  $\sqrt{\cdot}$  is the matrix square root (see [Galerne et al. 2011] for more details).

Figure 10 shows an application where two input power spectra  $(\mu, \nu)$  (computed using (23) from two input textures exemplars  $(f, g)$ ) are

interpolated using (6), and for each interpolation parameter  $t \in [0, 1]$  a new texture  $F$  is synthesized and displayed. Note that while the Q-Sinkhorn Algorithm 1 is provided for real PSD matrices, it extends verbatim to complex positive hermitian matrices (the matrix logarithm and exponential being defined the same way as for real matrices).

## 6 Conclusion

In this work, we have proposed a new static formulation for OT between tensor-valued measures. This formulation is an extension of the recently proposed unbalanced formulation of OT. A chief advantage of this formulation is that, once coupled with quantum entropic regularization, it leads to an effective numerical scheme, which is easily extended to the computation of barycenters.

## Acknowledgements

DTI data were provided by Franco Pestilli (NSF IIS 1636893; NIH ULTR001108) and the Human Connectome Project (NIH 1U54MH091657). The images for the texture synthesis experiments are from IPOL<sup>2</sup>. The images for the triangular meshing experiments are from Wikimedia.

Initial results in this paper were shared in a non-peer-reviewed pre-publication [Anonymous 2016].

<sup>2</sup>[www.ipol.im](http://www.ipol.im)

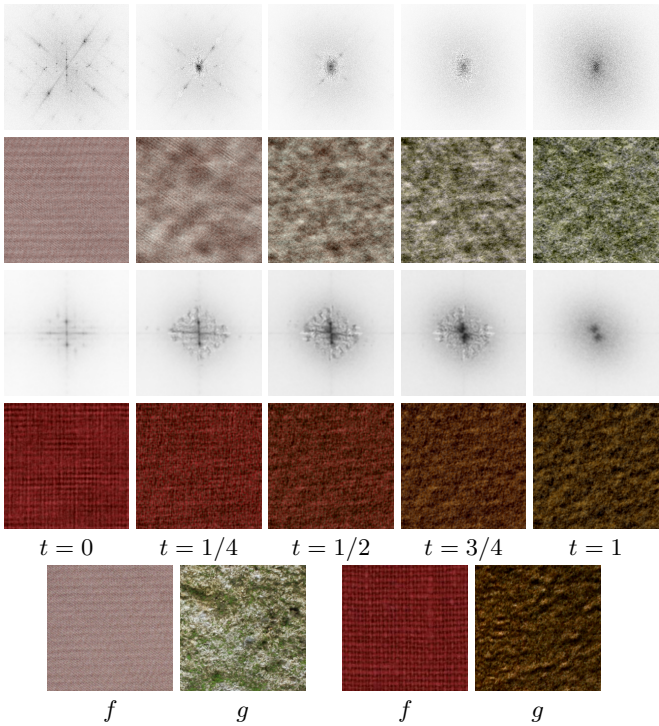


**Figure 10:** **Row 1 and 3:** display  $\text{tr}(\mu_t(x))$  where  $\mu_t$  are the interpolated power spectra. **Rows 2 and 4:** realizations of the Gaussian field parameterized by the power spectra  $\mu_t$ . **Row 5:** input texture exemplars from which  $(\mu_{t=0}, \mu_{t=1}) = (\mu, \nu)$  are computed.

- BONNEEL, N., VAN DE PANNE, M., PARIS, S., AND HEIDRICH, W. 2011. Displacement interpolation using Lagrangian mass transport. *ACM Trans. Graph.* 30, 6 (Dec.), 158:1–158:12.
- BOUGLEUX, S., PEYRÉ, G., AND COHEN, L. D. 2009. Image compression with anisotropic geodesic triangulations. In *Proc. of ICCV'09*, 2343–2348.
- BREGMAN, L. M. 1967. The relaxation method of finding the common point of convex sets and its application to the solution of problems in convex programming. *USSR comp. math. and math. phys.* 7, 3, 200–217.
- BRENIER, Y. 1991. Polar factorization and monotone rearrangement of vector-valued functions. *Comm. Pure Appl. Math.* 44, 4, 375–417.
- CARLEN, E. A., AND MAAS, J. 2014. An analog of the 2-Wasserstein metric in non-commutative probability under which the fermionic Fokker–Planck equation is gradient flow for the entropy. *Communications in Mathematical Physics* 331, 3, 887–926.
- CHANDRASEKARAN, V., AND SHAH, P. 2016. Relative entropy optimization and its applications. *Mathematical Programming*, 1–32.
- CHEN, Y., GEORGIOU, T. T., , AND TANNENBAUM, A. 2016. Distances and Riemannian metrics for multivariate spectral densities. *Preprint arXiv:1610.03041*.
- CHIZAT, L., PEYRÉ, G., SCHMITZER, B., AND VIALARD, F.-X. 2015. Unbalanced optimal transport: Geometry and Kantorovich formulation. *Preprint 1508.05216*, Arxiv.
- CHIZAT, L., PEYRÉ, G., SCHMITZER, B., AND VIALARD, F.-X. 2016. Scaling algorithms for unbalanced transport problems. *Preprint 1607.05816*, Arxiv.
- CHIZAT, L., SCHMITZER, B., PEYRÉ, G., AND VIALARD, F.-X. 2016. An interpolating distance between optimal transport and Fisher–Rao. *to appear in Foundations of Computational Mathematics*.
- CRANE, K., DESBRUN, M., AND SCHRÖDER, P. 2010. Trivial connections on discrete surfaces. In *Computer Graphics Forum*, vol. 29, Wiley Online Library, 1525–1533.
- CUTURI, M. 2013. Sinkhorn distances: Lightspeed computation of optimal transportation. In *Proc. NIPS*, vol. 26, 2292–2300.
- DEMARET, L., DYN, N., AND ISKE, A. 2006. Image compression by linear splines over adaptive triangulations. *Signal Processing* 86, 7, 1604–1616.
- DERICHE, R., TSCHUMPELÉ, D., LENGLER, C., AND ROUSSON, M. 2006. *Variational Approaches to the Estimation, Regularization and Segmentation of Diffusion Tensor Images*. Springer US, Boston, MA, 517–530.
- DHILLON, I. S., AND TROPP, J. A. 2008. Matrix nearness problems with Bregman divergences. *SIAM Journal on Matrix Analysis and Applications* 29, 4, 1120–1146.
- DRYDEN, I. L., KOLOYDENKO, A., AND ZHOU, D. 2009. Non-Euclidean statistics for covariance matrices, with applications to diffusion tensor imaging. *The Annals of Applied Statistics*, 1102–1123.
- DYKSTRA, R. L. 1983. An algorithm for restricted least squares regression. *J. Amer. Stat.* 78, 384, 839–842.

- 632 FROGNER, C., ZHANG, C., MOBAHI, H., ARAYA, M., AND POG-  
633 GIO, T. 2015. Learning with a Wasserstein loss. In *Advances in*  
634 *Neural Information Processing Systems*, vol. 28. 2044–2052.
- 635 GALERNE, B., GOUSSEAU, Y., AND MOREL, J.-M. 2011. Random  
636 phase textures: Theory and synthesis. *IEEE Transactions on*  
637 *image processing* 20, 1, 257–267.
- 638 HOTZ, I., FENG, L., HAGEN, H., HAMANN, B., JOY, K. I., AND  
639 JEREMIC, B. 2004. Physically based methods for tensor field  
640 visualization. IEEE Computer Society, 123–130.
- 641 JIANG, X., NING, L., AND GEORGIOU, T. T. 2012. Distances  
642 and Riemannian metrics for multivariate spectral densities. *IEEE*  
643 *Transactions on Automatic Control* 57, 7 (July), 1723–1735.
- 644 KANTOROVICH, L. 1942. On the transfer of masses (in Russian).  
645 *Doklady Akademii Nauk* 37, 2, 227–229.
- 646 KONDRATYEV, S., MONSAINGEON, L., AND VOROTNIKOV, D.  
647 2015. A new optimal transport distance on the space of finite  
648 Radon measures. Tech. rep., Pre-print.
- 649 KULIS, B., SUSTIK, M. A., AND DHILLON, I. S. 2009. Low-rank  
650 kernel learning with Bregman matrix divergences. *J. Mach. Learn.*  
651 *Res.* 10 (June), 341–376.
- 652 LAGAE, A., LEFEBVRE, S., COOK, R., DERROSE, T., DRETTAKIS,  
653 G., EBERT, D. S., LEWIS, J., PERLIN, K., AND ZWICKER,  
654 M. 2010. A survey of procedural noise functions. In *Computer*  
655 *Graphics Forum*, vol. 29, Wiley Online Library, 2579–2600.
- 656 LAGAE, A., LEFEBVRE, S., AND DUTRÉ, P. 2011. Improving  
657 Gabor noise. *IEEE Transactions on Visualization and Computer*  
658 *Graphics* 17, 8, 1096–1107.
- 659 LIERO, M., MIELKE, A., AND SAVARÉ, G. 2015. Optimal entropy-  
660 transport problems and a new Hellinger–Kantorovich distance  
661 between positive measures. *ArXiv e-prints*.
- 662 LIERO, M., MIELKE, A., AND SAVARÉ, G. 2016. Optimal transport  
663 in competition with reaction: The Hellinger–Kantorovich distance  
664 and geodesic curves. *SIAM Journal on Mathematical Analysis*  
665 48, 4, 2869–2911.
- 666 MONGE, G. 1781. Mémoire sur la théorie des déblais et des  
667 remblais. *Histoire de l'Académie Royale des Sciences*, 666–704.
- 668 NING, L., AND GEORGIOU, T. T. 2014. Metrics for matrix-valued  
669 measures via test functions. In *53rd IEEE Conference on Decision*  
670 *and Control*, IEEE, 2642–2647.
- 671 NING, L., GEORGIOU, T. T., AND TANNENBAUM, A. 2015. On  
672 matrix-valued Monge–Kantorovich optimal mass transport. *IEEE*  
673 *transactions on automatic control* 60, 2, 373–382.
- 674 PESTILLI, F., YEATMAN, J. D., ROKEM, A., KAY, K. N., AND  
675 WANDELL, B. A. 2014. Evaluation and statistical inference for  
676 human connectomes. *Nature methods* 11, 10, 1058–1063.
- 677 ROCKAFELLAR, R. T. 1970. *Convex analysis*. Princeton University  
678 Press.
- 679 RUBNER, Y., TOMASI, C., AND GUIBAS, L. J. 2000. The earth  
680 mover's distance as a metric for image retrieval. *International*  
681 *Journal of Computer Vision* 40, 2 (Nov.), 99–121.
- 682 SANTAMBROGIO, F. 2015. Optimal transport for applied mathe-  
683 maticians. *Progress in Nonlinear Differential Equations and their*  
684 *applications* 87.
- 685 SCHMITZER, B. 2016. Stabilized sparse scaling algorithms for  
686 entropy regularized transport problems. *arXiv:1610.06519*.
- 687 SHEWCHUK, J. 2002. What is a good linear finite element? Interpo-  
688 lation, conditioning, anisotropy, and quality measures (preprint).  
689 *University of California at Berkeley* 73.
- 690 SINKHORN, R. 1964. A relationship between arbitrary positive  
691 matrices and doubly stochastic matrices. *Ann. Math. Statist.* 35,  
692 876–879.
- 693 SOLOMON, J., DE GOES, F., PEYRÉ, G., CUTURI, M., BUTSCHER,  
694 A., NGUYEN, A., DU, T., AND GUIBAS, L. 2015. Convolutional  
695 Wasserstein distances: Efficient optimal transportation on  
696 geometric domains. *TOG* 34, 4 (July), 66:1–66:11.
- 697 TAKEMURA, H., CAIAFA, C. F., WANDELL, B. A., AND PESTILLI,  
698 F. 2016. Ensemble tractography. *PLoS Comput Biol* 12, 2,  
699 e1004692.
- 700 VAXMAN, A., CAMPEN, M., DIAMANTI, O., PANZZO, D.,  
701 BOMMES, D., HILDEBRANDT, K., AND BEN-CHEN, M. 2016.  
702 Directional field synthesis, design, and processing. *Comput.*  
703 *Graph. Forum* 35, 2, 545–572.
- 704 WANDELL, B. A. 2016. Clarifying human white matter. *Annual*  
705 *Review of Neuroscience*.
- 706 WEICKERT, J. 1998. *Anisotropic diffusion in image processing*,  
707 vol. 1. Teubner Stuttgart.